Chemical Science

ROYAL SOCIETY OF CHEMISTRY

EDGE ARTICLE

View Article Online
View Journal | View Issue

Cite this: *Chem. Sci.*, 2025, **16**, 16610

All publication charges for this article have been paid for by the Royal Society of Chemistry

Experimental determination of the magnetic anisotropy in five-coordinated Co(II) field-induced single molecule magnets

Hannah H. Slavensky, †[a] Vijay S. Parmar, †*[a] Sofie S. Leiszner, [a] Andreas M. Thiel,[a] Helene Lassen,[a] Stuart Calder, [b] Iurii Kibalin [c] and Bo B. Iversen *[a]

Magnetic anisotropy of the central metal atom is a crucial property of single molecule magnets (SMMs). Small structural changes can alter the magnetic properties, and accurate experimental methods to investigate magnetic anisotropy are therefore critical. Here, we investigate two five-coordinated Co(II) SMMs, [$CoCl_2$Cltpy] (**1**) and [$CoBr_2$Cltpy] (**2**) (Cltpy = 4′-chloro-2,2′:6′,2″-terpyridine), through multiple techniques. *Ab initio* theoretical calculations performed on the two compounds show that both possess axial magnetic anisotropy with the magnetic easy axis pointing towards one of the terminal halogen atoms. Theoretical calculations on SMMs are typically done on isolated molecular species, and to validate this approximation the magnetic anisotropy was further studied through experimental techniques. EPR measurements confirm an axial anisotropy of **1**, and magnetic measurements provide experimental Zero-Field Splitting (ZFS) parameters, showing that the values from theoretical calculations are slightly overestimated. The X-ray electron density determined from 20 K single-crystal synchrotron X-ray diffraction data provides estimated d-orbital populations also suggesting axial magnetic anisotropy in both systems, and furthermore suggesting a more pronounced axiality in **1** compared to **2**. This is in good agreement with the results obtained from both magnetic measurements and theoretical calculations. The magnetic anisotropy of **1** is quantified experimentally through polarized powder neutron diffraction *via* the site susceptibility method, confirming an axial magnetic anisotropy of the compound. A slight deviation in the easy axis direction is observed between experimental and theoretical results. This, together with the overestimation of the ZFS parameters from theoretical calculations, shows that experimental investigation of the magnetic anisotropy of SMMs is of high relevance.

Received 28th April 2025
Accepted 11th August 2025

DOI: 10.1039/d5sc03103f

rsc.li/chemical-science

Introduction

Single molecule magnets (SMMs) exhibit slow relaxation of magnetization thereby possessing an energy barrier for magnetic reversal.[1] Due to this property SMMs have potential applications in molecular spintronics and quantum computing.[2–5] The main developments of SMMs involve both 3d- and 4f-ion-based systems with high-performance molecules reaching blocking temperatures up to 80 K.[6–13] 3d-ion based SMMs have the advantage of a great tunability of the ground spin state *via* the crystal field, leading to strong magneto-structural correlations, and providing an abundance of possible SMM candidates. Small differences in the coordination environment of the central metal atom have been shown to alter the magnetic properties significantly.[14–16] This feature is a strong tool for creating systems with specific properties but also increases the demand for experimental techniques that can accurately determine the magnetic anisotropy of the systems.

The family of Co(II) based SMMs has been widely studied due to interesting properties of high energy barriers, and ambient stability when the coordination number of Co is four or higher, an important factor in the potential applications of these molecules.[10,17–30] The number of studied five-coordinated Co(II) SMMs are limited compared to four- and six-coordinated systems,[31] but is very interesting as they have shown high-performance SMM properties both in the trigonal bipyramidal and square pyramidal geometry (Table S15).[18,32–36] Due to strong magneto-structural correlations for these compounds where small deviations in the crystal field environment can change the magnetic anisotropy from easy-plane to easy-axis and *vice versa*[14,16,31] it is crucial to investigate these systems experimentally.

[a]*Department of Chemistry, Aarhus University, Langelandsgade 140, DK-8000 Aarhus C, Denmark. E-mail: vsp@chem.au.dk; bo@chem.au.dk*

[b]*Oak Ridge National Laboratory, Neutron Scattering Division, Oak Ridge, Tennessee 37831, USA*

[c]*Diffraction Group, Institut Laue-Langevin, 71 Avenue des Martyrs, 38042 Grenoble, France*

† Shared first authors.

The magnetic anisotropy of SMMs is often studied through fitting of DC magnetic measurements along with theoretical *ab initio* calculations, from which the ZFS-parameters, D and E, can be obtained, in addition to g-values and the g-tensor of the system, which provide information on the principal magnetic axes. The g-tensor is most often reported from theoretical calculations, and experimental determination of the g- or χ-tensor in SMMs is less common. Comparing the magnetic anisotropy obtained from theoretical calculations to the values from magnetic measurements should be done with some caution, as theoretical calculations typically are performed on an isolated molecule, thereby excluding intermolecular interactions and packing effects, to minimize the calculation costs and avoid overparameterization. In contrast, the experimental parameters obtained from magnetic measurements include all the effects present in the solid state. Due to these limitations of theoretical calculations, it is important to investigate the magnetic anisotropy of SMMs using experimental techniques, to ensure that correct information of the local magnetic anisotropy of the systems is obtained. Such techniques are, however, limited and rarely used in the field of molecular magnetism as they require considerable experimental sophistication. Examples are high-field and high-frequency electron paramagnetic resonance,[37] nuclear magnetic resonance,[38] cantilever torque magnetometry,[39] and inelastic neutron scattering.[40] In addition to these methods, polarized neutron diffraction is a strong experimental tool in the investigation of magnetic properties and has been utilized to obtain the local atomic magnetic susceptibility tensor *via* the site susceptibility method[41–43] for SMMs.[28,44–52] The method is usually applied to single crystal samples, which restricts the possible systems that can be investigated, due to the need for large single crystals with sizes larger than 1 mm^3. A recent study comparing the use of this technique on single crystal and powder samples was published by some of us, and it showed that powder samples can provide accurate determination of the magnetic susceptibility tensor.[28] This makes the site susceptibility method more applicable for obtaining experimental information on the magnetic anisotropy of SMMs.

X-ray electron density determination is another experimental technique that provides important information in the study of SMMs, even though the magnetic properties are not directly studied. Elaborate multipole modelling of the electron density determines the aspherical electron density features around the central metal atom making it possible to investigate the magneto-structural correlations present in SMMs through detailed metal–ligand bond analysis. Furthermore, the magnetic anisotropy can be explored through d-orbital population analysis of the central metal atom in 3d-ion based SMMs. X-ray electron density studies have recently been used in the field of SMMs to obtain d-orbital populations,[53–56] from which estimates of the ZFS were made.[28,57] Another study has explored and quantified the oblateness of the 4f valence experimental electron density in a Dy(III) SMM.[58]

As theoretical calculations provide a strong tool in the investigations of SMM properties and in the search for new high-performance compounds[59] it is important to establish the reliability between these theoretical results and the magnetic anisotropy obtained from experimental techniques. In this paper, we study the magnetic anisotropy of two air-stable five-coordinated Co(II) based SMMs, in which the Co(II) ion is coordinated to an NNN-based tridentate ligand and two terminal halide ligands, through different experimental techniques. No reported five-coordinated Co(II) based SMM has, to the best of our knowledge, shown zero-field SMM properties, and the two compounds are thus also expected to show slow relaxation of the magnetization only in the presence of a DC-field. The two compounds are studied through various magnetic measurements, electronic paramagnetic resonance (EPR) measurements, low temperature single crystal synchrotron X-ray diffraction, theoretical *ab initio* calculations, and polarized powder neutron diffraction, with the aim of investigating the magnetic anisotropy of the two compounds in detail and furthermore to compare the results obtained from experimental and theoretical methods.

Results and discussion

Synthesis and molecular structure

The two Co(II) complexes [$CoCl_2$Cltpy] (**1**) and [$CoBr_2$Cltpy] (**2**) (Cltpy = 4′-chloro-2,2′:6′,2″-terpyridine) were synthesized from the reaction of anhydrous $CoCl_2$ and $CoBr_2$, respectively, with Cltpy under ambient conditions (Scheme S1).[60] Green, air-stable crystals were obtained for **1** and **2** by vapor diffusion in diethyl ether (Fig. S1). Low-temperature high-resolution single-crystal X-ray diffraction (SC-XRD) data were collected at the BL02B1 beam line at SPring-8 synchrotron of **1** and **2** at 20 K (see SI for details). Both complexes crystallize in the monoclinic space group $P2_1/c$. Crystallographic information can be found in Table S5. From the high-quality SC-XRD data the structure of **1** and **2** is obtained (see Fig. 1, S18 and S19). The two compounds are isostructural, and the coordination environment around the penta-coordinated Co(II) ions are investigated through continuous shape measures[61] for both complexes (see Table S6), which show that the best description of the geometry of both compounds is a distorted square pyramidal geometry with one halogen in equatorial N_3 plane of the ligand and one halogen directly above to this plane.

The Co-N bond lengths are in the range from 2.086 Å to 2.152 Å for **1**, and from 2.080 Å to 2.154 Å for **2** (see Table S7 for all Co

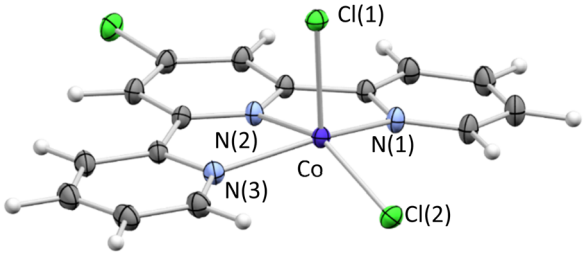

Fig. 1 Experimental SC-XRD structure of **1** at 20 K (90% probability ellipsoids). Atom colours: Co (dark blue), Cl (green), N (light blue), C (grey) and H (white). Complex **2** is isostructural to **1** but has two bromide ions bound to Co instead of two chloride ions.

bond lengths with uncertainties). The Co-Cl(**1**) bond perpendicular to the ligand plane has a bond length of 2.33944(2) Å, which is slightly longer than the equatorial Co-Cl(**2**) bond length of 2.29571(2) Å. The same trend is found for the Co-Br bonds in **2**, where the perpendicular Co-Br(**1**) bond has a length of 2.47487(5) Å, and the equatorial Co-Br(**2**) bond has a slightly shorter length of 2.45118(5) Å. The bond angles are very similar when comparing **1** and **2** (see Table S8), highlighting the isostructural relationship between the two structures. The molecules show π–π stacking within the unit cell (see Fig. S20 and S21) with the π–π stacking distances of 3.587 and 3.590 Å for **1** and **2** respectively. The nearest Co atoms are separated by 5.90794(2) Å in **1** and 5.87513(5) Å in **2**.

Theoretical calculations

The atomic positions obtained for **1** and **2** from SC-XRD were used to perform *ab initio* calculations with the Complete Active Space Self-Consistent Field (CASSCF) method and energies corrected with the *N*-electron Valence State Perturbation Theory (NEVPT2) in the ORCA software[62–64] (see SI for further details). Theoretical ZFS parameters and *g*-values obtained from the calculations are listed in Table 1, together with information on the directions of the three magnetic axes, shown in Fig. S2 for **1** and **2**.

For both **1** and **2**, a negative *D*-value is obtained indicating easy axis magnetic anisotropy for the two complexes. The non-zero value of *E* suggests a difference in the two hard axes of the system, which is also displayed in the *g*-values. For an axial system, the *g*-values normally follow the order $g_x = g_y < g_z$. The *g*-values follow the order $g_x < g_y \ll g_z$ and $g_x < g_y < g_z$, for **1** and **2** respectively, indicating that the magnetic anisotropy is in-between axial and tri-axial[54] with a more pronounced tri-axiality for **2**. The non-zero *E*-values for the compounds further indicate a mixing of M_S states within the lowest lying Kramers' Doublet (KD). The calculated composition of the KDs for **1** and **2** is:

$$\mathrm{KD1}(\mathbf{1}) = 0.71|(0), \pm3/2\rangle + 0.26|(1), \pm3/2\rangle + 0.02|(0), \pm1/2\rangle + 0.01|(2), \pm1/2\rangle$$

$$\mathrm{KD1}(\mathbf{2}) = 0.72|(0), \pm3/2\rangle + 0.21|(1), \pm3/2\rangle + 0.05|(0), \pm1/2\rangle + 0.02|(2), \pm1/2\rangle$$

The wave functions of the KDs consist mostly of contributions from $M_s = \pm3/2$ states, in good agreement with the negative *D*-value obtained for the systems. The small contributions of $M_s = \pm1/2$ states correlate well with the non-zero *E*-value, and as the $M_s = \pm1/2$ contribution is larger for **2** this agrees with the larger *E*-value for this compound, emphasizing its tri-axial magnetic anisotropy. The energies and wave-functions for higher-laying KDs are given in Tables S2 and S3. The direction of the magnetic axes of **1** and **2** are almost identical. As seen in Fig. S2 the magnetic easy axis (g_z) almost coincides with the Co-Cl/Br(**2**) bond. The two hard axes, g_x and g_y, point towards the Cl/Br-atom above the NNN-plane (with an angle of ∼30°) and towards the N(1) and N(3) atoms, respectively. The direction of the magnetic easy axis obtained for **1** and **2** is similar to the ones found for other square-pyramidal Co(II) based SMMs.[35,36,65] Based on the theoretical calculations, the magnetic anisotropy of **1** and **2** differ mostly by the size of the ZFS-parameters and *g*-values, whereas the direction of the easy axis is very similar. The theoretical results obtained for **1** and **2** will be compared to experimental results obtained by multiple techniques in the following sections, giving insights into the differences, if any, in results obtained from experiments and theory.

Table 1 Calculated and experimental magnetic parameters for **1** and **2**

Calcd/(fitted)	**1**($S = 3/2$)	**2**($S = 3/2$)
Parameters from SH model		
g_x	1.98/(2.49)	1.99/(2.42)
g_y	2.33/(2.49)	2.44/(2.42)
g_z	3.07/(2.86)	2.94/(2.76)
D (cm^{-1})	−78.87/(−55.27)	−60.61/(−48.71)
E (cm^{-1})	13.7/(16.19)	18.1/(15.38)
$E/\|D\|$	0.174/(0.29)	0.298/(0.31)
zj (cm^{-1})	(0.0082)	(−0.0135)
χ_{TIP} ($cm^3\ mol^{-1}$)	(4.41×10^{-4})	(8.0×10^{-4})
$R(\chi T) \times R(M)$	(3.4×10^{-3})	(7.9×10^{-5})
Parameters from GF model		
σ	(1.45(1))	(1.5)
λ (cm^{-1})	(−92)	(88.2)
B_2^0 (cm^{-1})	(−440(1))	(−283(2))
B_2^2 (cm^{-1})	(0.012)	(−63(2))
zj (cm^{-1})	(0.012)	(-0.005)
χ_{TIP} ($cm^3\ mol^{-1}$)	(1.4×10^{-3})	(1.2×10^{-3})
$R(\chi T) \times R(M)$	(0.342)	(0.778)

EPR measurements

X-band EPR measurements were performed on the powder sample of a magnetically diluted sample of 0.1% Co@[$ZnCl_2$(-Cltpy)] (**1a**) at 20 K (Fig. 2, see SI for additional information). The CASSCF/NEVPT2 computed energy gap between the ground and the first excited Kramers' doublet (∼5000 GHz, see Table S2) is very large with respect to the X-band EPR limits (9.7 GHz). Hence, only the ground Kramers' doublet is accessible for this analysis, and therefore a simplified effective spin 1/2 model was used to simulate the EPR spectrum using the EasySpin simulation package.[66] The EPR spectrum also contains hyperfine structure due to the magnetic ^{59}Co nucleus ($I = 7/2$). Upon fitting with the effective spin 1/2 model, effective *g* and A values were obtained as $g_1 = 1.35(5)$, $g_2 = 1.88(13)$, $g_3 = 7.59(1)$, $A_1 = 89$ MHz, $A_2 = 68$ MHz, $A_3 = 982.72$ MHz, which are in the range of previously reported values of such complexes.[36,67–69] Effective spin 1/2 values are also obtained from theoretical *ab initio* calculations (Table S1). The theoretical values calculated for **1** follow the same trend as the ones obtained from EPR (g_1, $g_2 \ll g_3$), with a small g_x value, a slightly larger g_y and then a very large g_z value, indicating an axial magnetic anisotropy of the compound. Furthermore, the difference in the g_x and g_y value observed in both EPR and theoretical calculations shows that

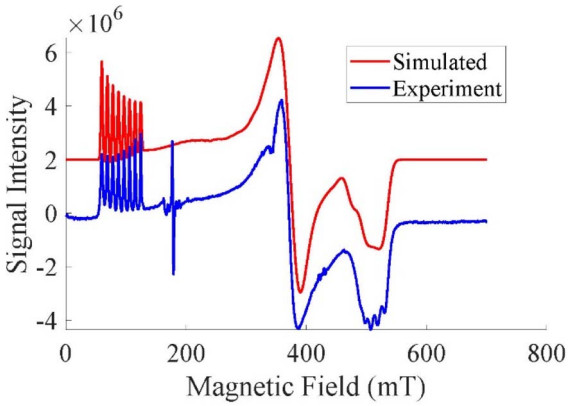

Fig. 2 EPR spectrum for **1** measured at a frequency of 9.7 GHz and a temperature of 20 K (blue line). Simulation (red line) was performed with effective spin 1/2 model using EasySpin package. The peak at 190 mT in the experimental data is attributed to the background (see Fig. S4). An offset on the *y*-axis is applied to the simulated curve for clarity.

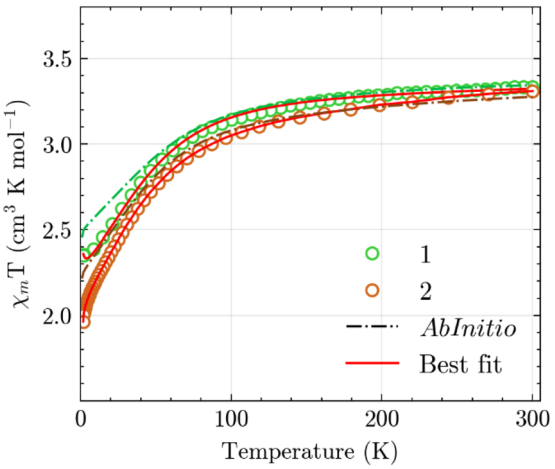

Fig. 3 Product of molar magnetic susceptibility and temperature against temperature for **1** (green) and **2** (brown). The dot-dashed lines represent theoretically calculated curves, and solid red lines represent the best fit with the Spin Hamiltonian approach using Phi program packages.

the two hard axes differ in properties (one being slightly easier to magnetize than the other). Looking at the calculated spin 1/2 values for **2**, these follow the same trend as for **1**, but with a smaller deviation of the smallest and largest values and a more significant difference between g_x and g_y., indicating a less pronounced axiality of the magnetic anisotropy of **2**.

Magnetic measurements

To investigate the magnetic properties, DC (direct current) and AC (alternating current) magnetic measurements were performed on powder samples of **1** and **2**. Powder X-ray diffraction (PXRD) measurements, ICP-OES and elemental analysis were performed on both compounds to ensure bulk phase purity of these samples (see Fig. S28 and S29).

The temperature dependence of the magnetic susceptibility of **1** and **2** was measured under a static magnetic field of 0.1 T in the temperature range of 1.8 K to 300 K. The product of the molar magnetic susceptibility and temperature, $\chi_M T$, shows values of 3.33 and 3.30 cm^3 K mol^{-1} for **1** and **2**, respectively, around room temperature (Fig. 3). These $\chi_M T$ values are significantly higher than the spin-only value (1.875 cm^3 K mol^{-1}, $S = 3/2$, $g = 2$) for high-spin Co(II) ions, indicating highly anisotropic Co(II) complexes with strong orbital contributions.[35,36,67,69,70] The $\chi_M T$ values of **1** and **2** change insignificantly upon lowering the temperature from 300 K to 100 K, thereafter decreasing rapidly below 100 K, reaching 2.36 and 2.1 cm^3 K mol^{-1} for **1** and **2**, respectively, at 2 K. The observed temperature dependent magnetic susceptibility at low temperature suggests significant magnetic anisotropy, likely arising from zero-field splitting. The $\chi_M T$ behaviour at lowest temperature varies from the results obtained from theoretical calculations for **1**, whereas it is similar to the calculated behaviour for **2**. The $\chi_M T$ product reaches a minimum value of 2.31 cm^3 K mol^{-1} around 3.5 K, thereafter, increasing slightly to 2.37 cm^3 K mol^{-1} at 1.8 K for **1**, suggesting mild ferromagnetic exchange coupling *via* intermolecular interactions ($zJ > 0$).[18,71–73] However, the temperature dependence of molar magnetic susceptibility under field cooled and zero-field cooled conditions overlap with no bifurcation or a peak in ZFC (Fig. S6) for both **1** and **2**.

Field dependent magnetic isotherms were measured for **1** and **2** from 0–7 T between temperatures 2–5 K and at 10 K (Fig. 4 and S7). The saturation magnetization at 2 K and 7 T is found to be 2.43 and 2.36 μ_B for **1** and **2**, respectively. The saturation magnetization at lowest temperature and highest field is lower than the expected spin-only value ($M_{sat} = g \times S \approx 3\ \mu_B$ for $g = 2$ and $S = 3/2$) and non-overlapping reduced magnetization curves (Fig. S7) for both **1** and **2** indicate magnetic anisotropy within the compounds. The deviation is within the observed range for similar complexes in the literature.[35,74,75]

Lower than calculated saturation magnetisation values confirm the presence of ZFS.[16,35,67,69–71] Therefore, the DC magnetic data was first modelled using the ZFS Spin Hamiltonian (SH) approach (see equation below) with added terms such as temperature independent paramagnetic (TIP) contributions and intermolecular field interactions contribution (zJ) as implemented in the Phi program package.[76] The temperature dependent magnetic susceptibility and field dependent magnetization data was simultaneously fitted to attain ZFS and g parameters for **1** and **2**. The static magnetic data could be satisfactorily fitted using the SH formalism with the parameters listed in Table 1 (resultant fitted curves in Fig. 3, 4 and S7). The $g_x = g_y$ restrain was used to restrict one of the g values to reduce to unphysical numbers while fitting, and not more than four parameters were refined at a time to avoid over-parameterization. These values are around the reported range in literature for similar complexes.[16,35,67,69–71] The fitted ZFS parameters are lower than the *ab initio* calculated values for both complexes. Overestimation of the ZFS parameters leading to low expected magnetization from *ab initio* theoretical calculations for five-coordinate high-spin Co(II) SMMs is not rare in the literature.[16,35,67,69–71]

$$\hat{H}_{SH} = D\left[\hat{S}_z^{\,2} - \frac{1}{3}S(S+1)\right] + E\left(\hat{S}_x^{\,2} + \hat{S}_y^{\,2}\right) + \mu_B \hat{S}\cdot\overline{\overline{g}}\cdot\vec{B}$$

The spin Hamiltonian approach to obtain the ZFS parameters and their meaning remain limited to orbitally non-degenerate ground state which is well separated from the excited states.[77] However, *ab initio* calculated CASSCF-NEVPT2 energies indicate lower ground and excited state gap. The Griffith-Figgis approach, which is usually applied to model static magnetic data of octahedral Co(II) high-spin complexes, although not ideal, can be utilised in this case since the psuodo-C_{4v} symmetry splitting is like an axial distortion effect in octahedral complexes.[69,77,78]

The GF Hamiltonian contains the angular momentum operators ($\hat{L}$, $\hat{L}_{x,y,z}$), spin–orbit coupling constant (λ) and the orbital reduction parameter (σ). Parameter σ accounts for the metal–ligand bond covalency (in some context) or other lower symmetry effects that alter the effective orbital angular momentum; it ranges between $0 > \sigma \geq -3/2$. The GF Hamiltonian also utilises the $B_2^{\,0}$ and $B_2^{\,2}$ parameters which describe the axial and rhombic distortions to the ideal geometry, respectively. The DC magnetisation (M *vs.* H) and magnetic susceptibility ($\chi_M T$ *vs.* T) data were simultaneously fitted for **1** and **2** using the GF model with the effect of TIP and molecular fields (zJ) included using Phi.[76] The resulting fitting parameters are shown in Table 1 and the fitted curves in Fig. S9 and S10. The fitted curves and residuals indicate slightly better fit with the SH model than the GF model. The D, E/D and $B_2^{\,0}$, $B_2^{\,2}$ parameters as extracted from the SH and GF models respectively, suggest a higher degree of axiality in **1** than **2** which is also the estimate from the *ab initio* calculations. The obtained temperature independent paramagnetic susceptibility and zJ values from the fitting suggest intermolecular exchange or long-range crystal effects which influence the static magnetic properties that are often unaccounted for in the *ab initio* calculations of such complexes. Interestingly, both models, GF and SH, suggest a positive zJ parameter for **1** which is rare in such complexes, confirming weak ferromagnetic interaction in **1**. Complex **1** is very similar to a previously reported field-induced SMM by Murugesu *et al.* ([Co(tPy)Cl_2]).[36] However, the introduction of the chloride on the terpyridine ligand enhances short contacts which affects the molecular packing in the structure. The nearest Co–Co distance in **1** is 5.90 Å *vs.* 7.68 Å in [Co(tPy)Cl_2]; similarly, the π–π stacking distance in **1** is 3.59 Å *vs.* 3.79 Å in [Co(tPy)Cl_2]. This closer packing of molecules with elevated short contacts in **1** may contribute towards weak ferromagnetic coupling at low temperature which was not reported for [Co(tPy)Cl_2].[36] Short range non-covalent interactions and close π–π stacking leading to weak ferromagnetic exchange have been observed in similar Co(II) field induced SMMs.[18,71–73] The ferromagnetic intermolecular interactions could be reduced by separating the magnetic centres further apart. A magnetically diluted sample, Co@Zn was synthesized having 1.14% of Co centres in the [Zn(CltPy)Cl_2] structure (magnetic dilution calculated *via* M *vs.* H curve at 2 K from 0–7 T for Co@Zn). The DC data (Fig. S8) for Co@Zn shows no increment of the $\chi_M T$ product at lowest temperature confirming that the very slight increment in $\chi_M T$ between 1.8–3 K that was observed in **1** is likely due to weakly ferromagnetic intermolecular interactions. Furthermore, a magnetic hysteresis loop of **1** was recorded at 1.8 K between −7 to 7 T (field sweep rate 100 Oe s^{-1}). The magnetic hysteresis loop (Fig. S8) for **1** remain closed at 1.8 K indicating no long-range magnetic ordering.

$$\hat{H}_{GF} = \sigma\lambda\hat{L}\cdot\hat{S} + \sigma^2 B_2^{\,0}\left(3\hat{L}_z^{\,2} - \hat{L}^2\right) + \sigma^2 B_2^{\,2}\left(\hat{L}_x^{\,2} - \hat{L}_y^{\,2}\right) + \mu_B\left(\sigma\hat{L} + 2\hat{S}\right)\cdot\vec{B}$$

AC

To probe the slow relaxation of the magnetization dynamics in **1** and **2**, the temperature and frequency dependencies of the AC susceptibility were measured between 2–8 K (see SI for details). Neither compound showed a peak in the out-of-phase component of the ac susceptibility at zero applied DC field likely due to strong quantum tunnelling of magnetization at zero field. Multiple applied DC fields were tested at 2 K to assess the field-induced slow relaxation of magnetization. Out-of-phase magnetic susceptibility peaks could be observed upon application of external field as low as 500 Oe. Further investigation was carried out under an applied field of 1000 Oe and out-of-phase susceptibility peaks could be observed up to 7.5 K for **1** and 5.25 K for **2** (Fig. 4) within the available AC frequency range. The obtained AC data under applied field was fitted using a generalized Debye model *via* the CCFIT2 software package (version 5.7.1)[74,75] to extract the relaxation times (τ) and their distribution with temperature (Table S4), described by α ($0 \leq \alpha \leq 1$). An α-value of 1 corresponds to an infinitely wide distribution of relaxation times, whereas an α-value of 0 represents relaxation with a single time constant. The relaxation profiles (τ^{-1} *vs.* T), Cole–Cole plots, and α *vs.* T plots are shown in Fig. 5, S11 and S12, respectively. The α value ranges from 0.016–0.17 for **1** indicating singular relaxation channel whereas it ranges from 0.008–0.3 for **2** with large uncertainties (due to noisy data). The relaxation rate against temperature for **1** is fitted against the equation below where the corresponding terms from left to right describe Direct, Raman, Orbach, and Quantum tunnelling of magnetization (QTM) relaxation processes, respectively, to extract the relaxation parameters.

$$\tau^{-1} = 10^{-D}\cdot T + 10^{-R}\cdot T^n + 10^{-A}\cdot e^{(-U_{eff}/k_B T)} + 10^{-Q}$$

Multiple combinations of the relaxation process were tried (Fig. S13) and adequate fits for **1** could be achieved with combinations of (1) Direct and Raman processes (Fig. 5) with parameters, $D = 2.268(9)$ $\log_{10}(s^{-1}\,K^{-1})$, $R = -1.10(3)$ $\log_{10}(s^{-1}\,K^{-n})$, $n = 6.71(4)$; (2) Orbach and direct processes with parameters, $U_{eff} = 40.6(7)$ K, $A = 7$, $D = 2.37(2)$ as well as with a combination of (3) Orbach, Raman and QTM processes having the parameters as $U_{eff} = 27$ K, $A = 2.8$, $R = -0.8(2)$, $n = 6.8$ (1), $Q = -2.67(1)$. Similar relaxation parameters, when Orbach process was involved, were observed for [Co(tPy)Cl_2][36] and other pentacoordinate Co(II) field-induced SMMs that have similar

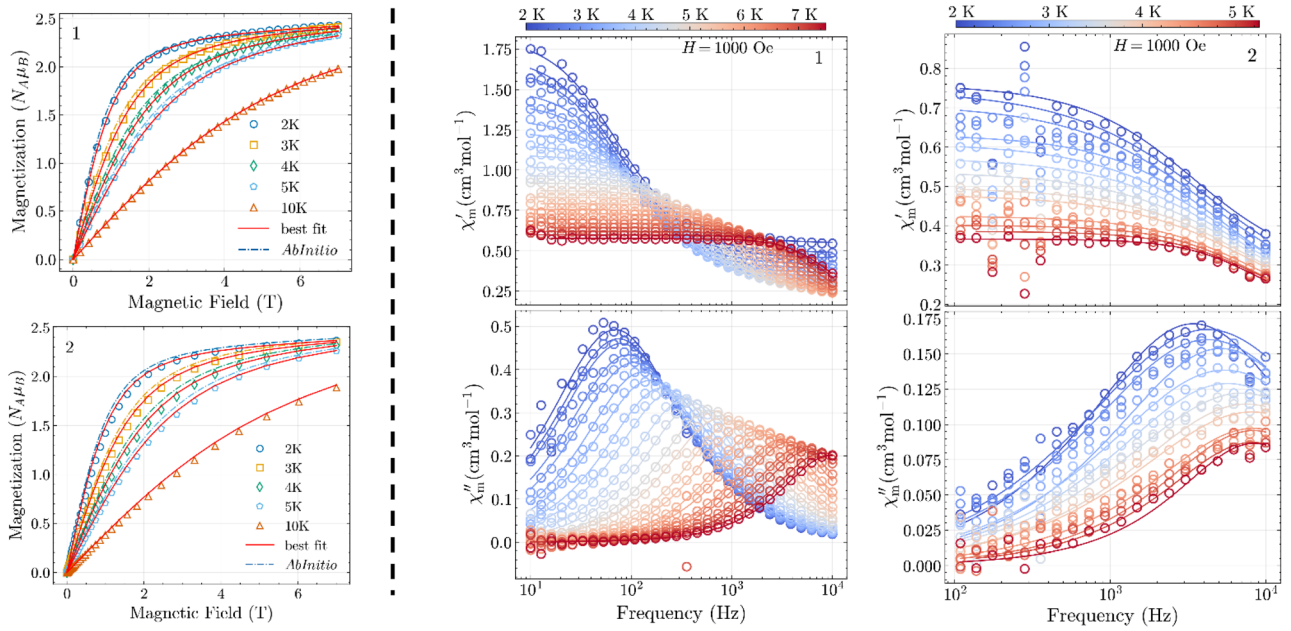

Fig. 4 (Left): Field dependent magnetization between 2–10 K for **1** (top-left) and **2** (bottom-left). The dot-dash lines represent theoretically calculated curves, and solid red lines represent the best fit with the Spin Hamiltonian approach. (Right): Temperature and frequency dependence of the in-phase (χ'_m, top) and out-of-phase component (χ''_m, bottom) of the molar magnetic susceptibility of **1** (centre) and **2** (right) under a 1000 Oe external magnetic field. The solid lines represent fits using the generalized Debye model.

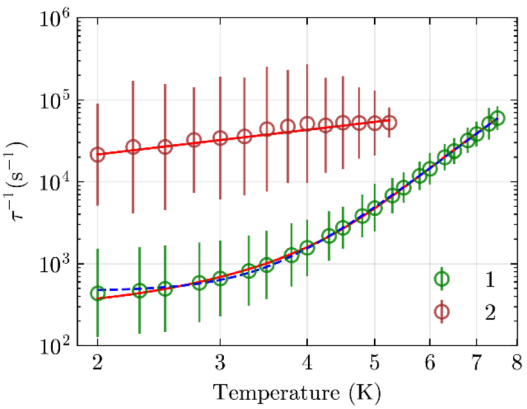

Fig. 5 Relaxation profiles of τ^{-1} *vs.* T for **1** (green circles) and **2** (brown circles). The solid lines show best fit profiles for **1** and **2**. The dashed blue line shows the best fit results for **1** including the Orbach, Raman and QTM relaxation pathways.

geometries (Table S15). The relaxation profile for **2** could be fitted with a direct process (Fig. 5) with parameter $D = 4.03(1)$ $\log_{10}(s^{-1}\,K^{-1})$. Complexes **1** and **2** differ notably from each other at lower temperature not only in their static magnetic properties but also in their dynamic properties as seen from their relaxation profiles in Fig. 5. The rates of relaxation in **2** are much faster than in **1** and remain faster with decreasing temperature. The relaxation mechanism changes at lower temperature from faster Raman to a direct mechanism for **1**. This difference in the preferred relaxation mechanisms arises most likely from the difference in the phonon density profiles of **1** and **2**, as moving from the lighter Cl ligand in **1** to the heavier Br ligand in **2** can affect the scale of the phonon energies. Furthermore, among the square pyramidal high-spin Co(II) field induced SMMs, the distance between the basal plane of the pyramid (formed by $N_3Cl(2)$ for **1** and $N_3Br(2)$ for **2**) and the Co centre also correlates with the D, E/D and U_{eff} values.[35,36] The distance between the basal plane and the Co centre is 0.494 Å and 0.477 Å for **1** and **2**, respectively; the bigger distance shows elevated U_{eff} values and $|D|$ values.[35,36]

Multipole models of the electron densities

To gain further insights into the coordination environment and its effect on the magnetic anisotropy of the Co(II) ion in the complexes, we have collected high-resolution X-ray diffraction data at the SPring8 synchrotron in Japan on single crystals of **1** and **2**. The data were collected at 20 K using a PILATUS X 1M CdTe detector. The initial analysis of the diffraction data on **1** revealed that the intensities of the strong reflections were generally underestimated (Fig. S15), a known issue when using a high flux beamline and this particular detector.[79] The underestimation was especially pronounced for the data collected on the single crystal of **1** due to its larger size and consequently stronger diffracted beam flux. As a result, we excluded data with $\sin\theta/\lambda$ values below 0.3 Å^{-1} for complex **1** and below 0.1 Å^{-1} for complex **2**. Although removing low-angle data is not ideal as they carry significant contributions from the valence electrons, it was deemed necessary in this case. Some caution should be taken when interpretating the results from the experimental model of the electron density of complex **1**. The SI contains additional information on the data collection strategy and details on the treatment of the underestimated intensities.

After performing the data reduction and solving the structure of both complexes, Multipole Models (MMs) of the electron density were obtained using the Hansen-Coppens formalism[80] (see SI for details). As the data sets were collected at a temperature of 20 K, it is expected that the compounds are in their ground electronic state, and the MMs are thus assumed to represent the electron density of this state only. The final experimental MMs for **1** and **2** have $R(F)$-factors of 0.93% and 0.95%, respectively, and the maximum and minimum residual densities are small being +0.42 e Å^{-3} and −0.39 e Å^{-3} for complex **1** and +0.37 e Å^{-3} and −0.38 e Å^{-3} for complex **2**. In addition, the fractal dimension plots[81] are featureless and parabolic in shape (Fig. S17), suggesting no systematic errors in neither data nor models. In addition to the two experimental MMs, theoretical MMs were obtained for both complexes by performing *ab initio* CASSCF calculations on each of the experimental molecular structures and then calculating theoretical structure factors.[82] The final theoretical MMs for **1** and **2** yielded $R(F)$ values of 0.23% and 0.16%, respectively, and both show low residual density below ±0.3 e Å^{-3} for both complexes. Using these MMs, we will explore the interactions between Co and the ligands in the two structures through the Quantum Theory of Atoms In Molecules (QTAIM).[83] In addition, we will estimate d-orbital populations of Co(II) and compare between the two complexes to get insights into their magnetic anisotropy.[57]

Topological analysis

Based on the MMs, critical points in the electron density have been calculated.[83,84] The Bond Critical Point (BCP) is particularly relevant, as it signifies the presence of chemical bonding. The full molecular graph with all the critical points for complex **1** is shown in Fig. 6, and a similar molecular graph for complex **2** is shown in Fig. S23. The molecular graphs for the two compounds resemble each other as expected for two isostructural compounds. Fig. 6 shows the presence of BCPs between all bonded atoms, but also a few additional ones between the halogen (Cl(2) in **1** and Br(2) in **2**) in the N_3-plane and the nearby H-atoms. The presence of interactions between H-atoms and the halogens bonded to electron withdrawing transition metals are well known.[85,86] The σ-bond from the halogen to the Co(II) ion causes a distortion of the electron density around the halogen, such that the electron density is increased equatorial to the Co–halogen bond, but decreased along the extension of the bond, referred to as the σ-hole. The positively charged H-atoms interact with this excess electron density equatorial to the Co–halogen bond, generating additional BCPs in the molecular graph.

Several topological properties can be evaluated at the BCPs, including the electron density, the Laplacian ($\nabla^2\rho(r)$), the eigenvalues of the matrix of the second order derivatives of the electron density referred to as the Hessian, the ellipticity of the bond and the energy densities (Table 2 and Tables S9–S12). The BCP properties for the three Co–N bonds in the two complexes are very similar. The small values of electron density at the Co-N BCPs combined with the positive Laplacian indicate that these interactions are closed shell interactions. The central Co-N(2) bond is slightly shorter than the other two in each complex and consequently has a larger value of electron density at the BCP.

Using the same criteria, the Co-halogen bonds in the two complexes also classify as closed shell interactions as expected from their ionic character. However, the Co-Br bonds possess more covalent character than the corresponding Co-Cl bonds, due to their larger electron density and smaller Laplacian at the BCP. This is also apparent from the 2D plots of the static deformation density in the $CoCl_2$ and $CoBr_2$ planes shown in Fig. 7. The static deformation density, $\Delta\rho(r)$, is the difference between the electron density from the Multipole Model (MM) and the Independent Atom Model (IAM), $\Delta\rho(r) = \rho_{MM}(r) - \rho_{IAM}(r)$, and therefore highlights the aspherical features of the electron density such as bonding and lone pair regions.[87] The plot of the static deformation density for compound **2** shows how the electron density on Br(1) is distorted towards Co seen from the blue lobe of excess electron density similar to that of N(2) which has its lone pair oriented towards Co. Br(2) on the other hand, shows the distortion of its electron density due to the σ-bond to Co, and the blue lobes on Br(2) perpendicular to the Co-Br(2) bond show the excess electron density that the two nearby H-atoms bond to. The presence of the sigma hole and increased electron density perpendicular to the halogen bonds is also seen in the plot of the static deformation density in the N_3 plane showing the Cltpy ligand (Fig. S24 and S25). Here, the electron density on the Cl of the ligand shows a similar distortion with a depletion of electron density in extension of the C–Cl bond and a concentration perpendicular to it. Comparisons of the plots of the static deformation density in the CoX_2 planes for **1** and **2** (Fig. 7) show that the Cl ions in **1** are

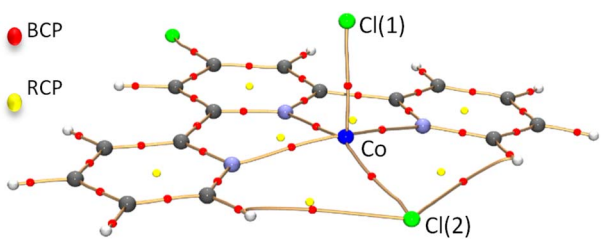

Fig. 6 Molecular graph of **1** showing the critical points in the electron density (bond critical points as red spheres and ring critical points as yellow spheres) and bond paths (golden cylinders). Atom colors: Co (dark blue), Cl (green), N (light blue), C (dark grey) and H (white).

Table 2 Topological properties at selected BCPs. The distance from the first atom to the BCP (d_1), the distance from the second atom to the BCP (d_2), the electron density at the BCP ($\rho(r)$) and the Laplacian at the BCP ($\nabla^2\rho(r)$). Only experimental values are shown. Values from the theoretical MM are shown in Table S6 and S8

Bond	d_1 (Å)	d_2 (Å)	$\rho(r)$ (e Å^{-3})	$\nabla^2\rho(r)$ (e Å^{-5})
Co-Cl(1)	1.0668	1.2762	0.21	4.79
Co-Cl(2)	1.0549	1.2468	0.24	5.29
Co-Br(1)	1.1166	1.3591	0.28	4.42
Co-Br(2)	1.1107	1.3425	0.27	4.13

more compact than the corresponding Br ions in **2**, as expected from the more ionic Co-Cl interaction. These plots show how the larger Br ions are more diffuse compared to the hard ion Cl, as expected from simple hard/soft acid/base chemistry.

d-Orbital populations

d-Orbital populations were derived from the MM using the approach developed by Holladay, Leung and Coppens,[88] and they are listed in Table 3. Presumably the more populated a d-orbital is, the lower its energy. The d-orbital populations are calculated with the following local coordinate system on Co: the *z*-axis towards Cl(1), the *x*-axis point towards N(1) and the *y*-axis is then roughly in the direction of Cl(2) (see Fig. S22). A similar coordinate system is chosen for **2**, but with axes towards the corresponding bromide atoms instead of chloride. According to the experimental MM of **1**, the energy ordering of the d-orbitals on Co are as follows (from lowest to highest energy): $d_{yz} < d_{xz} < d_{xy} \ll d_{z^2} < d_{x^2-y^2}$. This energy ordering fits well the expected d-orbital splitting for an ideal five-coordinated square pyramid configuration, which has an energy ordering of: $(d_{xz}, d_{yz}) < d_{xy} \ll d_{z^2} < d_{x^2-y^2}$. The only difference is the d_{yz} orbital being lower in energy than the d_{xz} orbital, and thereby lifting the degeneracy of these two orbitals. This is expected as the *y*-axis on Co is roughly oriented towards Cl(2), which is further from Co than the *N*-atoms in the *x*-direction. Additionally, Cl(2) is 0.321 Å below the N_3 plane, thereby stabilizing the d-orbitals with a y-component, explaining the lower energy of the d_{yz} orbital compared to d_{xz} in the experimental MM of **1**.

The obtained orbital splitting is favourable for a d_7 Co(II) complex to achieve a large magnetic anisotropy, as this will lead to the following high spin configuration: $d^2_{yz}d^2_{xz}d^1_{xy}d^1_{z^2}d^1_{x^2-y^2}$. The dominant coupling in regards of the first excited state will then be from d_{xz} to d_{xy} through the Lx operator,[54] leading us to expect a negative *D*-value for **1**. The energy ordering also fits well with the theoretical MM: $d_{yz} < (d_{xz}, d_{xy}) \ll d_{x^2-y^2} < d_{z^2}$, except from the lowering of the $d_{x^2-y^2}$ orbital energy compared to the d_{z^2} orbital. The energy ordering of d-orbitals from the theoretical MM on **2** resembles that from the theoretical MM on **1**. However, the experimental MM on **2** shows a different energy ordering: $(d_{yz}, d_{xz}) < (d_{xy}, d_{z^2}) < d_{x^2-y^2}$. With the two sets of degenerate orbitals, a positive *D*-value would be expected for this complex. However, a negative *D*-value is obtained from theoretical calculations, and the true d-orbital splitting of **2** is less certain. As the d_{xz} and d_{xy} orbitals are further apart in the MM of **2**, this suggests a smaller absolute *D*-value of **2** compared to **1**, and therefore a more pronounced axial magnetic anisotropy of **1** compared to **2**. This is in good agreement with both the results obtained from the theoretical calculations and fitting of magnetic data, in both cases we find that the absolute *D*-value is larger for **1** compared to **2**.

Table 3 d-orbital populations from experimental (first line) and theoretical (second line, italic) Multipole Models

d-orbital	$CoCl_2$Cltpy (**1**)	$CoBr_2$Cltpy (**2**)
$d_{x^2-y^2}$	15.8%	18.5%
	17.4%	*17.4%*
d_{z^2}	16.8%	19.1%
	16.7%	*16.6%*
d_{xy}	21.0%	19.0%
	21.6%	*21.4%*
d_{xz}	22.2%	21.6%
	21.5%	*21.5%*
d_{yz}	24.1%	21.8%
	22.7%	*23.2%*

Exploring magnetic anisotropy experimentally

The magnetic anisotropy of **1** has been explored throughout this paper with different techniques, which all serve as good indicators for the properties of the system, but all with some limitations. The magnetic measurements were performed on bulk samples, and from these results, the magnetic anisotropy is suggested to be axial, but with no information on direction or size. The theoretical calculations are based solely on the atomic positions from one molecule and thus do not consider intermolecular interactions or crystalline effects. The X-ray electron density gives detailed information on the bonding features of the complex including crystal effects but only qualitative information on magnetic anisotropy. To further quantify the magnetic anisotropy of **1** we use polarized powder neutron diffraction (PPND) and the site susceptibility method.[41–43] This technique provides the local atomic magnetic susceptibility tensor from experimental data as well as the direction of the easy axis and an estimate of the powder averaged magnetization. The technique has previously been used successfully to determine the atomic susceptibility tensors of SMMs.[44–51]

PPND data was obtained on a powder sample of **1** at the HB-2A/POWDER diffractometer of Oak Ridge National Laboratory (ORNL) at the high-flux isotope reactor (HFIR), at 2 K and with an applied magnetic field of 1 T using neutrons with wavelength of 2.41 Å. These measurement conditions ensure a linear regime of the magnetization (see Fig. 4). The synchrotron single-crystal X-ray structure was used to simulate nuclear structure factors and refinements of the model was performed in the CrysPy software.[89]

The flipping ratios obtained from the experiments are visualized as a sum- and difference pattern in Fig. S30 and S31. The signal-to-noise ratio for the difference pattern is low due to the challenges with measuring hydrogen-based samples with neutron

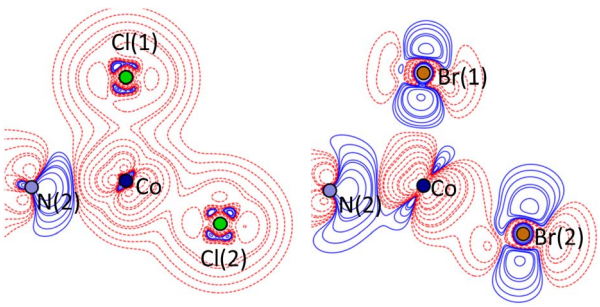

Fig. 7 Contour plots of the static deformation density in the $CoCl_2$ plane from the experimental MM of **1** (left) and in the $CoBr_2$ plane from the experimental MM of **2** (right). Blue is positive and red is negative, and the contour level is 0.05 e Å^{-3}.

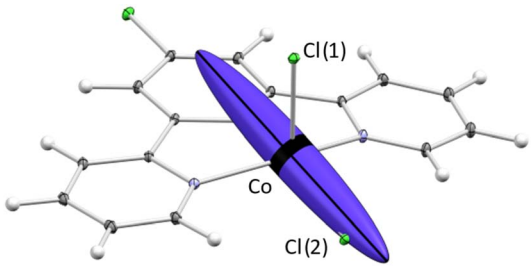

Fig. 8 Experimental magnetic susceptibility tensor obtained from PPND. The ellipsoid of the tensor is scaled arbitrarily with relative magnitudes corresponding to the relative eigenvalues in $\mu_B T^{-1}$.

scattering and isolated magnetic ions (further details are given in the SI). Consequently, only a few peaks are observed. However, we emphasize that we do indeed see clear scattering of both negative and positive intensities, and a meaningful local susceptibility tensor can be refined against the difference pattern.

A 2θ range of 10–67° was used in the PPND model, and initial refinements against both the sum- and difference-pattern were made on the background, shape parameters, asymmetry parameters, polarization factor, scale factor and beam offset. The refined values are then fixed, and the six parameters of the susceptibility tensor are refined against the difference pattern. During these refinements, restrictions on the susceptibility tensor were applied, to ensure positive eigenvalues, as negative eigenvalues are unphysical. Furthermore, preferred orientation of the crystallites in the sample due to the applied magnetic field is modelled with a modified March model.[89,90]

The obtained χ-tensor is visualized in Fig. 8, where the ellipsoid is scaled arbitrarily, and relative magnitudes correspond to the relative eigenvalues. The tensor clearly resembles a very axial system, with one axis that is easily magnetized and two hard axes. This confirms the predictions from both the experimental electron density analysis and theoretical *ab initio* calculations about axial magnetic anisotropy of **1**. The eigenvalues of the χ-tensor are refined to be 5.22(93), 0.06(8), and 0.16(65) $\mu_B T^{-1}$.

The eigenvectors of the χ-tensor represent the direction of the easy-axis and the two hard axes of the compound. All three eigenvectors are shown in Fig. S30. The easy-axis direction, *i.e.* the eigenvector corresponding to the largest eigenvalue, is shown in Fig. 9 together with the easy-axis obtained from the theoretical calculation. The experimental uncertainties on the obtained eigenvectors are expected to be in the same order of magnitude as the uncertainties of the eigenvalues. The angle between the two easy axes is 15.1°, which is comparable to other PPND/PND studies.[28,44,45,48]

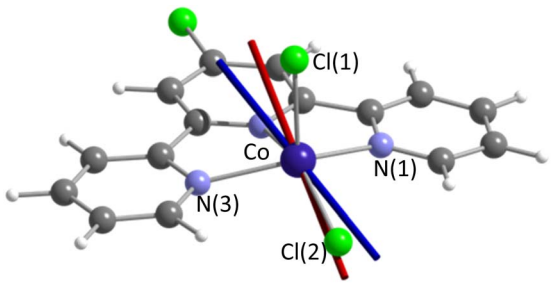

Fig. 9 Visualization of the magnetic easy axis of **1** from theoretical calculations (red) and PPND (blue).

This deviation between the easy-axis direction obtained from experiments and theory could be caused by intermolecular interactions, that are not included in the theoretical calculation, as recently discussed by Leiszner *et al.*[91]

An estimation of the powder average magnetization using the local anisotropy parameters can be made using the CrysPy software. The magnetic moment obtained for **1** is 1.813 μ_B/ion, in good agreement with the results obtained from bulk magnetization measurements of ~1.85 μ_B/ion at 2 K and 1 T (see Fig. 4). Overall, the PPND data gives comprehensive experimental insights to the magnetic anisotropy present in **1**, showing axial behaviour. The anisotropy of **2** has not been studied with PPND but based on the good agreement between PPND and the other reported results for **1**, the magnetic anisotropy of **2** is also expected to be axial with the easy axis in the direction of the Br(2) atom (Fig. S2).

Conclusions

The comprehensive study of the magnetic anisotropy of two Co(II) SMMs shows that they both possess axial magnetic anisotropy, supported by magnetic measurements, EPR measurements, analysis of the X-ray and theoretical electron density, theoretical calculations and polarized powder neutron diffraction. Large axial zero-field splitting parameters are obtained for both compounds from *ab initio* calculations, and the direction of the easy axis is shown to point towards one of the terminal halogen atoms. The experimental site susceptibility tensor is obtained from powder polarized neutron diffraction, showing good agreement with the direction obtained from theoretical calculations. The slight discrepancy of ~15° between the experimental and theoretical axes may be due to effects of intermolecular interactions.

Overall, the experimental and theoretical results show good agreements, suggesting that CASSCF/NEVPT2 results are reliable for investigating the magnetic anisotropy of these SMMs. However, as slight deviations are observed in ZFS parameters and direction of magnetic easy axis; we emphasize the importance of using experimental techniques to study the magnetic anisotropy of SMMs in detail.

A comparison of **1** and **2** shows a more pronounced axial magnetic anisotropy of **1**, both from theoretically obtained ZFS- and g-values and from analysis of d-orbital populations of the Co(II) ion of the complexes. This suggests that a more ionic terminal halogen ligand leads to a stronger axial magnetic anisotropy for this crystal field environment for Co(II) complexes, and that the crystal field indeed influences the magnetic properties of SMMs.

Experimental and theoretical methods

Synthesis

A solution of the ligand, Cltpy (4′-chloro-2,2′:6′,2″-terpyridine), (0.10 mmol, 26.8 mg) in dichloromethane (DCM) is added

dropwise to a solution of CoX_2 in MeOH (0.11 mmol, 14.3 mg for X = Cl, 0.13 mmol, 28.4 mg for X = Br). The slight excess of the metal precursor ensures the mononuclear pentacoordinate product as opposed to the hexacoordinated mononuclear or pentacoordinate dimer when using M : L : 1 : 1. Green crystals were obtained after a few days for both complexes by vapor diffusion in Et_2O at 4 °C.

Elemental analysis (CHN)

The elemental composition for the powder samples of **1** and **2** were measured five times by Elemental Analysensysteme GmbH using CHNS Vario MACRO cube analyser. For **1** calc.: C 45.318, H 2.535, N 10.570; found: C 45.35, H 2.545, N 10.56. For **2**, calc.: C 37.036, H 2.072, N 8.638; found: C 37.09, H 2.028, N 8.66.

FT-IR measurement was carried out with a PerkinElmer FTIR Spectrum-2 instrument in the range 400–4000 cm^{-1}.

FT-IR (solid, cm^{-1}) for **2**: 2975 s, 2927 m, 2880 w, 1450 s, 1420 s, 1380 s, 1323 w, 1274 s, 1088 s, 1046 s, 880 s, 803 s, 630 m.

ICP-OES (Inductively Coupled Plasma Optical Emission Spectrometry) measurements were carried out on a Spectro ARCOS ICP-OES equipped with a Burgener Nebulizer and Cyclonic Spray Chamber with an ASX-520 auto sampler. A standard series was measured on solutions with concentrations of 0.00999, 0.0999, 0.999, 4.995, 9.99, 49.95, 99.9, and 249.75 μg mL^{-1} of the first-row transition metals using ICP standards from PlasmaCAL.

Theoretical calculations

Ab initio theoretical calculations were performed using the ORCA software[62–64] with atomic positions obtained from the experimental electron density multipole model. The Complete Active Space Self-Consistent Field (CASSCF) method was used with the seven d-electrons of Co(II) in five active d-orbitals and the *N*-electron Valence State Perturbation Theory (NEVPT2) method was used for energy corrections. All ten $S = 3/2$ states and forty $S = 1/2$ states were included in the calculations and the def2-TZVP basis set was used. The spin–orbit coupling (SOC) was treated with the mean-field (SOMF) approximation.[92]

EPR

EPR measurements were performed at X-band (~9.7 GHz) using a Bruker Elexsys E580 spectrometer equipped with a Flexline MD5 dielectric resonator. The measurements were performed at the Novo Nordisk Foundation Copenhagen Pulse-EPR Facility. Simplified effective spin 1/2 model was used to simulate the EPR spectrum using the EasySpin simulation package in Matlab.[66]

Magnetic measurements

PXRD, Elemental analysis (CHN) and ICP-OES measurements were performed on the powder samples before the magnetic measurements to ensure bulk phase purity. Magnetic measurements were performed on a Quantum Design MPMS3 SQUID magnetometer (**1** and **2** DC measurements) and PPMS (**1** and **2** AC measurements). Crystals were ground into powder samples of **1** (18.5 mg and 11.89 mg) and **2** (14.97 mg) were used for the measurements. Raw moment data were corrected for sample shape and radial offset using the MPMS 3 Sample Geometry Simulator (see SI for further details).[93,94] Diamagnetic correction factors, calculated using the Pascal's constants[95] for the elements present in the complexes, -2.17×10^{-4} cm^3 mol^{-1} for **1** and -2.40×10^{-4} cm^3 mol^{-1} for **2**, were applied on the molar magnetic data for DC measurements. Field dependence of magnetization was recorded at a sweep rate of 100 Oe s^{-1} with stabilized field mode for both **1** and **2**. DC magnetic data was fitted using the Spin Hamiltonian (SH) and Griffith-Figgis Hamiltonian approach as implemented in the Phi program package.[76] For the AC data, no background correction was applied. AC data was fitted, and parameters were extracted using CCFIT2 program package (version 5.8.0).[74,75]

Single-crystal X-ray diffraction

X-ray diffraction data were collected for single crystals of **1** and **2** at the BL02B1 beam line at the SPring-8 synchrotron in Japan at 20 K with a wavelength of 0.2488 Å. The data were collected with a PILATUS X 1M CdTe detector[96] and ω scans were performed from 0 to 180° in steps of 0.1°, for fixed χ values of 0°, 20° or 40° and 2θ at 0° or −20° leading to 6 scans in total with 1800 frames in each. Attenuation of the incoming beam was not used for either experiment, which led to a known problem of the Pilatus X 1M CdTe detector with a too strong diffracted beam flux.[97] We treated this by introducing an extinction correction and cutting off the data with $\sin\theta/\lambda$ below 0.3 $Å^{-1}$ for 1 and below 0.1 $Å^{-1}$ for 2 in the multipole modelling in XD2016.[96] For additional details see the SI.

An offset in 2θ was observed for the $2\theta = -20°$ scans in both data sets. This was accounted for by changing the beam center position in these three scans. See SI for additional details. Initial unit cell determination was performed in APEX5 (ref. 97) and the integration was done using SAINT.[98]

SADABS[99] was used for scaling and absorption correction, the reflections were merged using SORTAV,[100] and XPREP[101] was used to determine the space group and prepare the input file to solve the structure. Finally, the structure was solved using SHELXT[102] in the Olex2 GUI.[103] The refined structure in Olex2 was used as the starting point for data treatment in XD2016.[96]

Multipole model of the electron density

The modelling in XD2016 is based on the Hansen and Coppens Multipole Model (MM),[80] which partitions the electron density of an atom, $\rho_{atom}(r)$, into three components: the spherical core density, the spherical valence density and the aspherical valence density:

$$\rho_{atom}(r) = P_c\rho_c(r) + P_v\kappa^3\rho_v(\kappa r) + \sum_{l=0}^{l_{max}} \kappa'^3 R_l\left(\kappa' r\right) \sum_{m=0}^{l} P_{lm\pm} d_{lm\pm}(\theta,\varphi)$$

where P_c, P_v and $P_{lm\pm}$ are the population parameters of the core, spherical valence and aspherical valence respectively. κ and κ' are the radial scaling parameters that allow for expansion and

contraction of the density. See the SI for further details on the MM refinements.

Polarized powder neutron diffraction

PPND data was collected at the HB-2A/POWDER diffractometer of Oak Ridge National Laboratory (ORNL) at the high-flux isotope reactor (HFIR) on 2 g of a powdered sample of 1. Data was collected at 2 K with an applied magnetic field of 1 T and with neutrons with a wavelength of 2.41 Å. The obtained flipping ratios were refined in the CrysPy software.[89]

Author contributions

H·H. S. carried out the synthesis, collected and analysed the PPND data, performed the theoretical calculations, contributed to the multipole modelling of the ED, and wrote the initial manuscript. V. P. Optimised the synthesis for the mononuclear pentacoordinate product and synthesised the magnetically diluted analogues, performed elemental analysis (CHN) and FTIR. Collected and analysed magnetic and EPR data. Contributed to the computational analysis of the magnetic data and contributed to the manuscript drafts and revisions. S.·S. L. carried out multipole modelling of the ED. A. M. T. collected the PPND data and did initial analysis. H. L. carried out initial synthesis, magnetic measurements and theoretical calculations. S. C. collected and contributed to analysis of PPND data. I. K. contributed to analysis of PPND data. B.·B. I. conceptualized the study, supervised experiments and analyses, obtained funding and edited the manuscript. All authors have given approval to the final version of the manuscript.

Conflicts of interest

There are no conflicts to declare.

Data availability

Raw data were generated at multiple instrumentation facilities. Derived data supporting the findings of this study are available from the corresponding author BBI on request.

CCDC 2451203 and 2451204 contain the supplementary crystallographic data for this paper.[104,105]

Supplementary Information containing further details of magnetic and EPR characterization, crystallography, multipole modelling, theoretical calculations and the refinement of PPND data available. See DOI: **https://doi.org/10.1039/d5sc03103f**.

Acknowledgements

The study was supported by the Villum Foundation (25861), the Danish Ministry for Higher Education and Sciences (Q-MAT lighthouse), Aarhus University Research Foundation, the Danish National Research Foundation (DNRF189), the Novo Nordisk Foundation, the Carlsberg Foundation and Danscatt. Jacob Overgaard is thanked for initial conceptualisation and discussion. This research used resources at the High Flux Isotope Reactor, a DOE Office of Science User Facility operated by the Oak Ridge National Laboratory. The beam time was allocated to HB-2A/POWDER on proposal number IPTS-28520.1. The authors would like to acknowledge the staff at the BL02B1 beamline at SPring-8 for measuring and providing the single-crystal diffraction data, Jacob Svane for collecting PXRD data, and Kim-Khuong Huynh for help with collecting magnetic data. We thank the Copenhagen Pulse EPR Facility, supported by a Research Infrastructure – Large Equipment and Facilities grant (NNF21OC0068806) from the Novo Nordisk Foundation. The numerical results presented in this work were obtained at the Centre for Scientific Computing, Aarhus.[64]

Notes and references

1 R. Sessoli, D. Gatteschi, A. Caneschi and M. A. Novak, Magnetic Bistability in a Metal-Ion Cluster, *Nature*, 1993, **365**, 141–143.
2 R. E. Winpenny, Quantum information processing using molecular nanomagnets as qubits, *Angew. Chem., Int. Ed.*, 2008, **47**, 7992–7994.
3 D. Gatteschi, R. Sessoli and J. Villain, *Molecular nanomagnets*, Oxford University Press, Oxford, New York, 2006.
4 M. N. Leuenberger and D. Loss, Quantum computing in molecular magnets, *Nature*, 2001, **410**, 789–793.
5 L. Bogani and W. Wernsdorfer, Molecular spintronics using single-molecule magnets, *Nat. Mater.*, 2008, **7**, 179–186.
6 F. S. Guo, B. M. Day, Y. C. Chen, M. L. Tong, A. Mansikkamaki and R. A. Layfield, Magnetic hysteresis up to 80 kelvin in a dysprosium metallocene single-molecule magnet, *Science*, 2018, **362**, 1400–1403.
7 C. A. P. Goodwin, F. Ortu, D. Reta, N. F. Chilton and D. P. Mills, Molecular magnetic hysteresis at 60 kelvin in dysprosocenium, *Nature*, 2017, **548**, 439–442.
8 P. C. Bunting, M. Atanasov, E. Damgaard-Moller, M. Perfetti, I. Crassee, M. Orlita, J. Overgaard, J. van Slageren, F. Neese and J. R. Long, A linear cobalt(II) complex with maximal orbital angular momentum from a non-Aufbau ground state, *Science*, 2018, **362**, 7319.
9 J. M. Zadrozny, D. J. Xiao, M. Atanasov, G. J. Long, F. Grandjean, F. Neese and J. R. Long, Magnetic blocking in a linear iron(I) complex, *Nat. Chem.*, 2013, **5**, 577–581.
10 Y. Rechkemmer, F. D. Breitgoff, M. van der Meer, M. Atanasov, M. Hakl, M. Orlita, P. Neugebauer, F. Neese, B. Sarkar and J. van Slageren, A four-coordinate cobalt(II) single-ion magnet with coercivity and a very high energy barrier, *Nat. Commun.*, 2016, **7**, 10467.
11 C. A. Gould, K. R. McClain, D. Reta, J. G. C. Kragskow, D. A. Marchiori, E. Lachman, E. S. Choi, J. G. Analytis, R. D. Britt, N. F. Chilton, B. G. Harvey and J. R. Long, Ultrahard magnetism from mixed-valence dilanthanide complexes with metal-metal bonding, *Science*, 2022, **375**, 198–202.
12 F. S. Guo, B. M. Day, Y. C. Chen, M. L. Tong, A. Mansikkamaki and R. A. Layfield, A Dysprosium Metallocene Single-Molecule Magnet Functioning at the Axial Limit, *Angew. Chem., Int. Ed.*, 2017, **56**, 11445–11449.

13 J. D. Rinehart and J. R. Long, Exploiting single-ion anisotropy in the design of f-element single-molecule magnets, *Chem. Sci.*, 2011, **2**, 2078–2085.
14 H. H. Cui, H. J. Xu, M. X. Zhang, S. C. Luo, W. Tong, M. Wang, T. M. Sun, L. Chen and Y. F. Tang, Magnetic Anisotropy from Easy-Plane to Easy-Axial in Square Pyramidal Cobalt(II) Single-Ion Magnets, *Cryst. Growth Des.*, 2022, **22**, 2742–2748.
15 R. F. Higgins, B. N. Livesay, T. J. Ozumerzifon, J. P. Joyce, A. K. Rappé and M. P. Shores, A family of related Co(II) terpyridine compounds exhibiting field induced single-molecule magnet properties, *Polyhedron*, 2018, **143**, 193–200.
16 I. Nemec, H. Liu, R. Herchel, X. Q. Zhang and Z. Trávnícek, Magnetic anisotropy in pentacoordinate 2,6-bis(arylazanylidene-1-chloromethyl)pyridine cobalt(II) complexes with chlorido co-ligands, *Synth. Met.*, 2016, **215**, 158–163.
17 M. Murrie, Cobalt(II) single-molecule magnets, *Chem. Soc. Rev.*, 2010, **39**, 1986–1995.
18 T. Jurca, A. Farghal, P. H. Lin, I. Korobkov, M. Murugesu and D. S. Richeson, Single-molecule magnet behavior with a single metal center enhanced through peripheral ligand modifications, *J. Am. Chem. Soc.*, 2011, **133**, 15814–15817.
19 J. Vallejo, I. Castro, R. Ruiz-Garcia, J. Cano, M. Julve, F. Lloret, G. De Munno, W. Wernsdorfer and E. Pardo, Field-induced slow magnetic relaxation in a six-coordinate mononuclear cobalt(II) complex with a positive anisotropy, *J. Am. Chem. Soc.*, 2012, **134**, 15704–15707.
20 Y. Y. Zhu, C. Cui, Y. Q. Zhang, J. H. Jia, X. Guo, C. Gao, K. Qian, S. D. Jiang, B. W. Wang, Z. M. Wang and S. Gao, Zero-field slow magnetic relaxation from single Co(II) ion: a transition metal single-molecule magnet with high anisotropy barrier, *Chem. Sci.*, 2013, **4**, 1802–1806.
21 S. Gómez-Coca, D. Aravena, R. Morales and E. Ruiz, Large magnetic anisotropy in mononuclear metal complexes, *Coord. Chem. Rev.*, 2015, **289**, 379–392.
22 A. K. Mondal, T. Goswami, A. Misra and S. Konar, Probing the Effects of Ligand Field and Coordination Geometry on Magnetic Anisotropy of Pentacoordinate Cobalt(II) Single-Ion Magnets, *Inorg. Chem.*, 2017, **56**, 6870–6878.
23 S. Vaidya, P. Shukla, S. Tripathi, E. Riviere, T. Mallah, G. Rajaraman and M. Shanmugam, Substituted *versus* Naked Thiourea Ligand Containing Pseudotetrahedral Cobalt(II) Complexes: A Comparative Study on Its Magnetization Relaxation Dynamics Phenomenon, *Inorg. Chem.*, 2018, **57**, 3371–3386.
24 H. H. Cui, F. Lu, X. T. Chen, Y. Q. Zhang, W. Tong and Z. L. Xue, Zero-Field Slow Magnetic Relaxation and Hysteresis Loop in Four-Coordinate Co(II) Single-Ion Magnets with Strong Easy-Axis Anisotropy, *Inorg. Chem.*, 2019, **58**, 12555–12564.
25 S. Tripathi, S. Vaidya, K. U. Ansari, N. Ahmed, E. Riviere, L. Spillecke, C. Koo, R. Klingeler, T. Mallah, G. Rajaraman and M. Shanmugam, Influence of a Counteranion on the Zero-Field Splitting of Tetrahedral Cobalt(II) Thiourea Complexes, *Inorg. Chem.*, 2019, **58**, 9085–9100.
26 A. Sarkar, S. Dey and G. Rajaraman, Role of Coordination Number and Geometry in Controlling the Magnetic Anisotropy in Fe(II) , Co(II) , and Ni(II) Single-Ion Magnets, *Chem.–Eur. J.*, 2020, **26**, 14036–14058.
27 J. N. Giraldo, J. Hruby, S. Vavreckova, O. F. Fellner, L. Havlicek, D. Henry, S. de Silva, R. Herchel, M. Bartos, I. Salitros, V. T. Santana, P. Barbara, I. Nemec and P. Neugebauer, Tetracoordinate Co(II) complexes with semi-coordination as stable single-ion magnets for deposition on graphene, *Phys. Chem. Chem. Phys.*, 2023, **25**, 29516–29530.
28 S. K. Gupta, H. H. Nielsen, A. M. Thiel, E. A. Klahn, E. Feng, H. B. Cao, T. C. Hansen, E. Lelievre-Berna, A. Gukasov, I. Kibalin, S. Dechert, S. Demeshko, J. Overgaard and F. Meyer, Multi-Technique Experimental Benchmarking of the Local Magnetic Anisotropy of a Cobalt(II) Single-Ion Magnet, *JACS Au*, 2023, **3**, 429–440.
29 R. Mitsuhashi, S. Hosoya, T. Suzuki, Y. Sunatsuki, H. Sakiyama and M. Mikuriya, Hydrogen-bonding interactions and magnetic relaxation dynamics in tetracoordinated cobalt(ii) single-ion magnets, *Dalton Trans.*, 2019, **48**, 395–399.
30 U. Albold, H. Bamberger, P. P. Hallmen, J. van Slageren and B. Sarkar, Strong Exchange Couplings Drastically Slow Down Magnetization Relaxation in an Air-Stable Cobalt(II)-Radical Single-Molecule Magnet (SMM), *Angew. Chem., Int. Ed.*, 2019, **58**, 9802–9806.
31 H. H. Cui, M. M. Ding, X. D. Zhang, W. Lv, Y. Q. Zhang, X. T. Chen, Z. Wang, Z. W. Ouyang and Z. L. Xue, Magnetic anisotropy in square pyramidal cobalt(II) complexes supported by a tetraazo macrocyclic ligand, *Dalton Trans.*, 2020, **49**, 14837–14846.
32 R. Ruamps, L. J. Batchelor, R. Guillot, G. Zakhia, A. L. Barra, W. Wernsdorfer, N. Guihéry and T. Mallah, Ising-type magnetic anisotropy and single molecule magnet behaviour in mononuclear trigonal bipyramidal Co(II) complexes, *Chem. Sci.*, 2014, **5**, 3418–3424.
33 A. Dey, J. Ali, S. Moorthy, J. F. Gonzalez, F. Pointillart, S. K. Singh and V. Chandrasekhar, Field induced single ion magnet behavior in Co(II) complexes in a distorted square pyramidal geometry, *Dalton Trans.*, 2023, **52**, 14807–14821.
34 J. Acharya, A. Sarkar, P. Kumar, V. Kumar, J. Flores Gonzalez, O. Cador, F. Pointillart, G. Rajaraman and V. Chandrasekhar, Influence of ligand field on magnetic anisotropy in a family of pentacoordinate Co(II) complexes, *Dalton Trans.*, 2020, **49**, 4785–4796.
35 V. Thangaraj, D. Sartini, D. Borah, D. Chauhan, V. Sharma, L. Sorace, G. Rajaraman, M. Perfetti and M. Shanmugam, Quantifying Magnetic Anisotropy of Series of Five-Coordinate Co(II) Ions: Experimental and Theoretical Insights, *Adv. Sci.*, 2025, **12**, e2415624.
36 F. Habib, O. R. Luca, V. Vieru, M. Shiddiq, I. Korobkov, S. I. Gorelsky, M. K. Takase, L. F. Chibotaru, S. Hill, R. H. Crabtree and M. Murugesu, Influence of the ligand

field on slow magnetization relaxation *versus* spin crossover in mononuclear cobalt complexes, *Angew. Chem., Int. Ed.*, 2013, **52**, 11290–11293.

37 A. N. Bone, C. N. Widener, D. H. Moseley, Z. Liu, Z. Lu, Y. Cheng, L. L. Daemen, M. Ozerov, J. Telser, K. Thirunavukkuarasu, D. Smirnov, S. M. Greer, S. Hill, J. Krzystek, K. Holldack, A. Aliabadi, A. Schnegg, K. R. Dunbar and Z. L. Xue, Applying Unconventional Spectroscopies to the Single-Molecule Magnets, Co(PPh(3))(2) X(2) (X=Cl, Br, I): Unveiling Magnetic Transitions and Spin-Phonon Coupling, *Chem.–Eur. J.*, 2021, **27**, 11110–11125.

38 Y. Zhang, D. Krylov, M. Rosenkranz, S. Schiemenz and A. A. Popov, Magnetic anisotropy of endohedral lanthanide ions: paramagnetic NMR study of MSc(2) N@C(80)-I(h) with M running through the whole 4f row, *Chem. Sci.*, 2015, **6**, 2328–2341.

39 M. Perfetti, G. Cucinotta, M. E. Boulon, F. El Hallak, S. Gao and R. Sessoli, Angular-resolved magnetometry beyond triclinic crystals part II: torque magnetometry of Cp*ErCOT single-molecule magnets, *Chem.–Eur. J.*, 2014, **20**, 14051–14056.

40 S. E. Stavretis, M. Atanasov, A. A. Podlesnyak, S. C. Hunter, F. Neese and Z. L. Xue, Magnetic Transitions in Iron Porphyrin Halides by Inelastic Neutron Scattering and *Ab Initio* Studies of Zero-Field Splittings, *Inorg. Chem.*, 2015, **54**, 9790–9801.

41 A. Gukasov and P. J. Brown, Determination of atomic site susceptibility tensors from polarized neutron diffraction data, *J. Phys. Condens. Matter*, 2002, **14**, 8831–8839.

42 A. Gukasov and P. J. Brown, Determination of atomic site susceptibility tensors from neutron diffraction data on polycrystalline samples, *J. Phys. Condens. Matter*, 2010, **22**, 502201.

43 E. Lelièvre-Berna, A. S. Wills, E. Bourgeat-Lami, A. Dee, T. Hansen, P. F. Henry, A. Poole, M. Thomas, X. Tonon, J. Torregrossa, K. H. Andersen, F. Bordenave, D. Jullien, P. Mouveau, B. Guérard and G. Manzin, Powder diffraction with spin polarized neutrons, *Meas. Sci. Technol.*, 2010, **21**, 055106.

44 E. A. Klahn, C. Gao, B. Gillon, A. Gukasov, X. Fabreges, R. O. Piltz, S. D. Jiang and J. Overgaard, Mapping the Magnetic Anisotropy at the Atomic Scale in Dysprosium Single-Molecule Magnets, *Chem.–Eur. J.*, 2018, **24**, 16576–16581.

45 S. Tripathi, S. Vaidya, N. Ahmed, E. A. Klahn, H. B. Cao, L. Spillecke, C. Koo, S. Spachmann, R. Klingeler, G. Rajaraman, J. Overgaard and M. Shanmugam, Structure-property correlation in stabilizing axial magnetic anisotropy in octahedral Co(II) complexes, *Cell Rep. Phys. Sci.*, 2021, **2**, 100404.

46 K. Ridier, A. Mondal, C. Boilleau, O. Cador, B. Gillon, G. Chaboussant, B. Le Guennic, K. Costuas and R. Lescouezec, Polarized Neutron Diffraction to Probe Local Magnetic Anisotropy of a Low-Spin Fe(III) Complex, *Angew. Chem., Int. Ed.*, 2016, **55**, 3963–3967.

47 K. Ridier, B. Gillon, A. Gukasov, G. Chaboussant, A. Cousson, D. Luneau, A. Borta, J. F. Jacquot, R. Checa, Y. Chiba, H. Sakiyama and M. Mikuriya, Polarized Neutron Diffraction as a Tool for Mapping Molecular Magnetic Anisotropy: Local Susceptibility Tensors in Co(II) Complexes, *Chem.–Eur. J.*, 2016, **22**, 724–735.

48 E. A. Klahn, E. Damgaard-Moller, L. Krause, I. Kibalin, A. Gukasov, S. Tripathi, A. Swain, M. Shanmugam and J. Overgaard, Quantifying magnetic anisotropy using X-ray and neutron diffraction, *Iucrj*, 2021, **8**, 833–841.

49 E. A. Klahn, A. M. Thiel, R. B. Degn, I. Kibalin, A. Gukassov, C. Wilson, A. B. Canaj, M. Murrie and J. Overgaard, Magnetic anisotropies of Ho(III) and Dy(III) single-molecule magnets experimentally determined *via* polarized neutron diffraction, *Dalton Trans.*, 2021, **50**, 14207–14215.

50 O. Iasco, Y. Chumakov, F. Guégan, B. Gillon, M. Lenertz, A. Bataille, J.-F. Jacquot and D. Luneau, Mapping the Magnetic Anisotropy inside a Ni4 Cubane Spin Cluster Using Polarized Neutron Diffraction, *Magnetochemistry*, 2017, **3**, 25.

51 A. Borta, B. Gillon, A. Gukasov, A. Cousson, D. Luneau, E. Jeanneau, I. Ciumacov, H. Sakiyama, K. Tone and M. Mikuriya, Local magnetic moments in a dinuclear Co2+complex as seen by polarized neutron diffraction:Beyond the effective spin-12model, *Phys. Rev. B: Condens. Matter Mater. Phys.*, 2011, **83**, 184429.

52 D. Luneau and B. Gillon, Polarized Neutron Diffraction: An Excellent Tool to Evidence the Magnetic Anisotropy-Structural Relationships in Molecules, *Magnetochemistry*, 2021, **7**, 158.

53 M. K. Thomsen, A. Nyvang, J. P. S. Walsh, P. C. Bunting, J. R. Long, F. Neese, M. Atanasov, A. Genoni and J. Overgaard, Insights into Single-Molecule-Magnet Behavior from the Experimental Electron Density of Linear Two-Coordinate Iron Complexes, *Inorg. Chem.*, 2019, **58**, 3211–3218.

54 E. Damgaard-Moller, L. Krause, H. Lassen, L. A. Malaspina, S. Grabowsky, H. Bamberger, J. McGuire, H. N. Miras, S. Sproules and J. Overgaard, Investigating Complex Magnetic Anisotropy in a Co(II) Molecular Compound: A Charge Density and Correlated *Ab Initio* Electronic Structure Study, *Inorg. Chem.*, 2020, **59**, 13190–13200.

55 M. Craven, M. H. Nygaard, J. M. Zadrozny, J. R. Long and J. Overgaard, Determination of d-Orbital Populations in a Cobalt(II) Single-Molecule Magnet Using Single-Crystal X-ray Diffraction, *Inorg. Chem.*, 2018, **57**, 6913–6920.

56 S. S. Leiszner, K. Chakarawet, J. R. Long, E. Nishibori, K. Sugimoto, J. A. Platts and J. Overgaard, Electron Density Analysis of Metal-Metal Bonding in a Ni(4) Cluster Featuring Ferromagnetic Exchange, *Inorg. Chem.*, 2023, **62**, 192–200.

57 E. Damgaard-Moller, L. Krause, K. Tolborg, G. Macetti, A. Genoni and J. Overgaard, Quantification of the Magnetic Anisotropy of a Single-Molecule Magnet from the Experimental Electron Density, *Angew. Chem., Int. Ed.*, 2020, **59**, 21203–21209.

58 C. Gao, A. Genoni, S. Gao, S. Jiang, A. Soncini and J. Overgaard, Observation of the asphericity of 4f-electron density and its relation to the magnetic anisotropy axis in single-molecule magnets, *Nat. Chem.*, 2020, **12**, 213–219.
59 L. A. Mariano, V. H. A. Nguyen, V. Briganti and A. Lunghi, Charting Regions of Cobalt's Chemical Space with Maximally Large Magnetic Anisotropy: A Computational High-Throughput Study, *J. Am. Chem. Soc.*, 2024, **146**, 34158–34166.
60 G. Q. Zhang, J. Tan, Y. Z. Zhang, C. Ta, S. Sanchez, S. Y. Cheng, J. A. Golen and A. L. Rheingold, Syntheses, structures and cytotoxicity of cobalt(II) complexes with 4′-chloro-2,2′:6′,2″-terpyridine, *Inorg. Chim. Acta*, 2015, **435**, 147–152.
61 M. Llunell, D. Casanova, J. Cirera, P. Alemany and S. Alvarez, *SHAPE Program for the Stereochemical Analysis of Molecular Fragments by Means of Continuous Shape Measures and Associated Tools, Version 2.1, Departament de Química Física*, Departament de Química Inorgànica, and Institut de Química Teòrica i Computacional - Universitat de Barcelona, 2013.
62 F. Neese, The ORCA program system, *Wiley Interdiscip. Rev. Comput.*, 2012, **2**, 73–78.
63 F. Neese, Software update: the ORCA program system, version 4.0, *Wiley Interdiscip. Rev. Comput.*, 2018, **8**, e1327.
64 F. Neese, F. Wennmohs, U. Becker and C. Riplinger, The ORCA quantum chemistry program package, *J. Chem. Phys.*, 2020, **152**, 224108.
65 Y. Cui, Y. Ge, Y. Li, J. Tao, J. Yao and Y. Dong, Single-ion magnet behavior of two pentacoordinate CoII complexes with a pincer ligand 2,6-bis(imidazo[1,5-a] pyridin-3-yl) pyridine, *Struct. Chem.*, 2019, **31**, 547–555.
66 S. Stoll and A. Schweiger, EasySpin, a comprehensive software package for spectral simulation and analysis in EPR, *J. Magn. Reson.*, 2006, **178**, 42–55.
67 S. Gomez-Coca, A. Urtizberea, E. Cremades, P. J. Alonso, A. Camon, E. Ruiz and F. Luis, Origin of slow magnetic relaxation in Kramers ions with non-uniaxial anisotropy, *Nat. Commun.*, 2014, **5**, 4300.
68 E. Y. Misochko, A. V. Akimov, D. V. Korchagin, J. Nehrkorn, M. Ozerov, A. V. Palii, J. M. Clemente-Juan and S. M. Aldoshin, Purely Spectroscopic Determination of the Spin Hamiltonian Parameters in High-Spin Six-Coordinated Cobalt(II) Complexes with Large Zero-Field Splitting, *Inorg. Chem.*, 2019, **58**, 16434–16444.
69 J. Juráková, J. Dubnická Midlíková, J. Hrubý, A. Kliuikov, V. T. Santana, J. Pavlik, J. Moncoľ, E. Čižmár, M. Orlita, I. Mohelský, P. Neugebauer, D. Gentili, M. Cavallini and I. Šalitroš, Pentacoordinate cobalt(ii) single ion magnets with pendant alkyl chains: shall we go for chloride or bromide?, *Inorg. Chem. Front.*, 2022, **9**, 1179–1194.
70 F. E. Mabbs and D. J. Machin, *Magnetism and transition metal complexes*, Chapman and Hall; distributed in the U.S.A. by Halsted Press, New York, London, 1973.
71 C. Rajnák, J. Titiš, J. Miklovič, G. E. Kostakis, O. Fuhr, M. Ruben and R. Boča, Five mononuclear pentacoordinate Co(II) complexes with field-induced slow magnetic relaxation, *Polyhedron*, 2017, **126**, 174–183.
72 I. Nemec, R. Herchel and Z. Trávníček, Ferromagnetic coupling mediated by Co…π non-covalent contacts in a pentacoordinate Co(II) compound showing field-induced slow relaxation of magnetization, *Dalton Trans.*, 2016, **45**, 12479–12482.
73 C. Rajnák, J. Titis, O. Fuhr, M. Ruben and R. Boca, Single-Molecule Magnetism in a Pentacoordinate Cobalt(II) Complex Supported by an Antenna Ligand, *Inorg. Chem.*, 2014, **53**, 8200–8202.
74 D. Reta and N. F. Chilton, Uncertainty estimates for magnetic relaxation times and magnetic relaxation parameters, *Phys. Chem. Chem. Phys.*, 2019, **21**, 23567–23575.
75 W. J. A. Blackmore, G. K. Gransbury, P. Evans, J. G. C. Kragskow, D. P. Mills and N. F. Chilton, Characterisation of magnetic relaxation on extremely long timescales, *Phys. Chem. Chem. Phys.*, 2023, **25**, 16735–16744.
76 N. F. Chilton, R. P. Anderson, L. D. Turner, A. Soncini and K. S. Murray, PHI: a powerful new program for the analysis of anisotropic monomeric and exchange-coupled polynuclear d- and f-block complexes, *J. Comput. Chem.*, 2013, **34**, 1164–1175.
77 R. Boča, *Theoretical foundations of molecular magnetism*, Elsevier, 1999.
78 G. K. Gransbury, M. E. Boulon, R. A. Mole, R. W. Gable, B. Moubaraki, K. S. Murray, L. Sorace, A. Soncini and C. Boskovic, Single-ion anisotropy and exchange coupling in cobalt(ii)-radical complexes: insights from magnetic and *ab initio* studies, *Chem. Sci.*, 2019, **10**, 8855–8871.
79 L. Krause, K. Tolborg, T. B. E. Gronbech, K. Sugimoto, B. B. Iversen and J. Overgaard, Accurate high-resolution single-crystal diffraction data from a Pilatus3 X CdTe detector, *J. Appl. Crystallogr.*, 2020, **53**, 635–649.
80 N. K. Hansen and P. Coppens, Electron Population Analysis of Accurate Diffraction Data 6. Testing Aspherical Atom Refinements on Small-Molecule Data Sets, *Acta Crystallogr. A*, 1978, **34**, 909–921.
81 K. Meindl and J. Henn, Foundations of residual-density analysis, *Acta Crystallogr. A*, 2008, **64**, 404–418.
82 A. Genoni, On the use of the Obara-Saika recurrence relations for the calculation of structure factors in quantum crystallography, *Acta Crystallogr., Sect. A:Found. Adv.*, 2020, **76**, 172–179.
83 R. F. W. Bader, *Atoms in Molecules: A Quantum Theory*, Clarendon Press, 1990.
84 P. L. A. Popelier, *Atoms in Molecules: An Introduction*, Prentice Hall, 2000.
85 T. Clark, M. Hennemann, J. S. Murray and P. Politzer, Halogen bonding: the sigma-hole. Proceedings of "Modeling interactions in biomolecules II", Prague, September 5th-9th, 2005, *J. Mol. Model.*, 2007, **13**, 291–296.
86 J. Y. C. Lim and P. D. Beer, Sigma-Hole Interactions in Anion Recognition, *Chem*, 2018, **4**, 731–783.
87 D. Stalke, Meaningful structural descriptors from charge density, *Chem.–Eur. J.*, 2011, **17**, 9264–9278.

88 A. Holladay, P. Leung and P. Coppens, Generalized Relations between D-Orbital Occupancies of Transition-Metal Atoms and Electron-Density Multipole Population Parameters from X-Ray-Diffraction Data, *Acta Crystallogr. A*, 1983, **39**, 377–387.
89 I. A. Kibalin and A. Gukasov, Local magnetic anisotropy by polarized neutron powder diffraction: Application of magnetically induced preferred crystallite orientation, *Phys. Rev. Res.*, 2019, **1**, 033100.
90 W. A. Dollase, Correction of Intensities for Preferred Orientation in Powder Diffractometry - Application of the March Model, *J. Appl. Crystallogr.*, 1986, **19**, 267–272.
91 S. S. Leiszner, M. Perfetti, E. Damgaard-Moller, Y. S. Chen and B. B. Iversen, The effect of second coordination sphere interactions on the magnetic anisotropy of transition metals, *Dalton Trans.*, 2024, **53**, 19246–19255.
92 F. Neese, Efficient and accurate approximations to the molecular spin-orbit coupling operator and their use in molecular g-tensor calculations, *J. Chem. Phys.*, 2005, **122**, 34107.
93 Quantum Design, *Accuracy of the Reported Moment: Sample Shape Effects, Application 1500-015, Rev. A0*, 2010.
94 G. Morrison and H.-C. zur Loye, Simple correction for the sample shape and radial offset effects on SQUID magnetometers: Magnetic measurements on Ln2O3 (Ln=Gd, Dy, Er) standards, *J. Solid State Chem.*, 2015, **221**, 334–337.
95 G. A. Bain and J. F. Berry, Diamagnetic corrections and Pascal's constants, *J. Chem. Educ.*, 2008, **85**, 532–536.
96 A. M. Volkov, P, L. J. Farrugia, C. Gatti, P. Mallinson, T. Richter and T. Koritsanszky, XD2016 - A Computer Program Package for Multipole Refinement, *Topological Analysis of Charge Densities and Evaluation of Intermolecular Energies from Experimental and Theoretical Structure Factors*, 2016.
97 *APEX5 v2023.9-2*, Bruker AXS Inc, Madison, Wisconsin, USA, 2023.
98 Bruker, *SAINT-Plus Integration Engine v8.40B*, Bruker AXS Inc, Madison, Wisconsin, USA, 2013.
99 L. Krause, R. Herbst-Irmer, G. M. Sheldrick and D. Stalke, Comparison of silver and molybdenum microfocus X-ray sources for single-crystal structure determination, *J. Appl. Crystallogr.*, 2015, **48**, 3–10.
100 R. H. Blessing, Outlier treatment in data merging, *J. Appl. Crystallogr.*, 1997, **30**, 421–426.
101 XPREP, *Bruker AXS*, 2014.
102 G. M. Sheldrick, SHELXT - integrated space-group and crystal-structure determination, *Acta Crystallogr., Sect. A:Found. Adv.*, 2015, **71**, 3–8.
103 O. V. Dolomanov, L. J. Bourhis, R. J. Gildea, J. A. K. Howard and H. Puschmann, OLEX2: a complete structure solution, refinement and analysis program, *J. Appl. Crystallogr.*, 2009, **42**, 339–341.
104 H. H. Slavensky, V. S. Parmar, S. S. Leiszner, A. M. Thiel, H. Lassen, S. Calder, I. Kibalin and B. B. Iversen, CCDC 2451203, Experimental Crystal Structure Determination, 2025, DOI: **10.5517/ccdc.csd.cc2n8p2q**.
105 H. H. Slavensky, V. S. Parmar, S. S. Leiszner, A. M. Thiel, H. Lassen, S. Calder, I. Kibalin and B. B. Iversen, CCDC 2451204, Experimental Crystal Structure Determination, 2025DOI: **10.5517/ccdc.csd.cc2n8p3r**.